PII: S0955-2219(98)00022-3

0955-2219/98/$—see front matter

Electron Spectroscopic Imaging and Fine Probe EDX Analysis of Liquid Phase Sintered Ceramics

Lena K. L. Falk

Department of Physics, Chalmers University of Technology, S-412 96 Göteborg, Sweden

(Received 12 November 1997; revised version received 15 January 1998; accepted 2 February 1998)

Abstract

This paper is focussed on high resolution imaging and microanalysis of two classes of liquid phase sintered ceramic materials, α and duplex α/β sialons and α-SiC ceramics. The microstructures were characterized in a FEGTEM equipped with surrounding interactive instrumentation for EDX and EELS analysis and electron energy filtering, and special attention was paid to the intergranular microstructure and the variation in local chemical composition. The α and duplex α/β sialon ceramics had been fabricated from balanced starting powder mixtures corresponding to the α-sialon composition $R_{0.4}Si_{10.2}Al_{1.8}O_{0.6}N_{15.4}$ (R = Sm, Dy or Yb) and the β-sialon composition $Si_{5.4}Al_{0.6}O_{0.6}N_{7.4}$. The α-SiC ceramics had been pressureless sintered or hot isostatically pressed with smaller additions of Al_2O_3 and Y_2O_3. Combined high resolution analytical and spatial information was obtained from electron spectroscopic images recorded around the C K, N K, O K, Al $L_{2,3}$ and rare earth element $N_{4,5}$ edges in the electron energy loss spectrum. Residual glassy grain boundary films rich in O and cations originating from the metal oxide/nitride additives were present at all characterized grain boundaries. High resolution imaging and elemental maps computed from the electron energy filtered images showed intergranular film thicknesses in the range 1·5 to 2·3 nm. The results imply that the intergranular film thickness in the sialon microstructures is dependent upon the particular grain boundary and the local chemistry as well as the α′ stabilizing cation. Elemental concentration profiles obtained by stepwise fine probe EDX analysis across α′/α′, α′/β′ and β′/β′ sialon grain boundaries revealed significant variations in the local α′ and β′ substitution levels, both within and between analysed grains. Concentration gradients within the sialon and α-SiC grains, associated with the different grain boundaries, were not detected.

1 Introduction

Structural ceramics based on the SiC and α- and β-Si_3N_4 structures are potential high strength materials for applications at ambient and high temperatures.[1–7] The interatomic bonding in the SiC and Si_3N_4 structures is strongly covalent, and the structures contain small, comparatively closely packed atoms which gives a large number of strong bonds per unit volume. This results in a combination of good inherent properties such as high strength, a high value of Youngs modulus, good oxidation and corrosion resistance, low thermal expansion and a relatively good thermal conductivity.

The strongly covalent bonding results also in extremely low self diffusivities at temperatures below that where appreciable decomposition of the ceramic compound starts. The fabrication of dense ceramics from SiC and α- and β-Si_3N_4 raw materials requires, therefore, a sintering additive that promotes densification, and at the same time inhibits the decomposition of the ceramic compound.[1–4,7–11] The additives will, however, generally introduce an intergranular microstructure that has a conclusive influence upon the properties of the liquid phase sintered ceramic material and may thereby determine the potential for different structural applications.[1–7,12–18] Refractory secondary phases and strong intergranular bonding are required for creep resistance and high strength at

elevated temperatures. On the other hand, activation of different toughening mechanisms such as crack deflection and bridging and micro-cracking rely upon 'sufficiently weak' interfaces. It becomes, hence, important to control the intergranular volume and its structure and chemistry. This requires imaging and analysis of down to, and even less than, nanometer sized regions in order to establish relationships between fabrication process, microstructure and properties.

Recent developments in analytical electron microscopy enable a detailed structural and chemical analysis of fine scale microstructural features. The optical performance of a modern transmission electron microscope (TEM) equipped with a field emission gun (FEG) makes it possible to form electron probes with a full width at half maximum (FWHM) of around one nanometer or less, and with sufficiently high currents for point analysis by energy dispersive X-ray spectroscopy (EDX) or electron energy loss spectroscopy (EELS). This instrumentation thus provides a powerful tool in combining fine probe microanalysis and high resolution imaging techniques.

The correlation of chemical information to structure in the TEM has generally been obtained by EDX or EELS when a focussed probe is stepped across the thin foil. The development of imaging filters that separate the contributions from electrons with different energies has made it possible to obtain high resolution two-dimensional chemical information from electron spectroscopic images.[19–23] Electron energy filtering can also be used in order to improve the contrast of images and diffraction patterns by removing the contribution from inelastic scattering.[19,20] Energy filtered TEM images and diffraction patterns are formed and detected in parallel which makes the acquisition time comparatively short.

This paper will focus on high resolution microanalysis in combination with high resolution imaging of two classes of liquid phase sintered ceramic materials: α and duplex α/β sialons and α-SiC ceramics. The microstructures were characterized in a FEGTEM equipped with surrounding interactive instrumentation for EDX and EELS analysis and electron energy filtering. Special attention has been paid to the intergranular microstructure and the variation in local chemical composition.

2 Liquid Phase Sintered Ceramics

2.1 Densification

Dense ceramic materials based on the SiC and α- and β-Si_3N_4 structures may be formed by sintering of powder compacts containing additions of metal oxides and/or nitrides.[1–4,7,9–11,24–26] These additives participate in liquid phase formation above relevant eutectic temperatures; the additives react with the inherent surface silica present on the SiC or Si_3N_4 starting powder particles, and some of the SiC or Si_3N_4, whereby an oxycarbide or oxynitride liquid phase sintering medium is formed. Densification is achieved through particle rearrangement in the liquid and solution followed by reprecipitation of the solid phase. Densification rate and grain growth, and thereby the grain shape and size distributions of the sintered material, depend upon liquid volume and chemistry at the sintering temperature.[14,17,24,27–30]

The microstructure of the sintered material consists of SiC, Si_3N_4 or sialon grains and intergranular phases Fig. 1. Secondary crystalline phases may partition from the liquid phase sintering medium during densification, or form during a post-densification heat treatment at lower temperatures; a number of the secondary crystalline phases that may form in these systems are not stable at the high densification temperature.[1,4,7,10,25,26,31–33] A certain volume fraction of the liquid is, however, generally retained as a residual intergranular glassy phase.

It has been demonstrated that Si_3N_4 powder compacts without additives may be fully densified by hot isostatic pressing (HIP); the inherent surface silica layer provides a sufficient sintering additive in combination with the applied high pressure.[28] HIP of SiC powder compacts containing smaller additions of Al_2O_3 and/or Y_2O_3 ($\leq$3 wt%) results, on the other hand, in a limited decomposition of the SiC according to the reaction

$$SiC + 2/3M_2O_3 \rightarrow SiO_2 + 4/3M + C \qquad (1)$$

where M stands for Al and/or Y.[25]

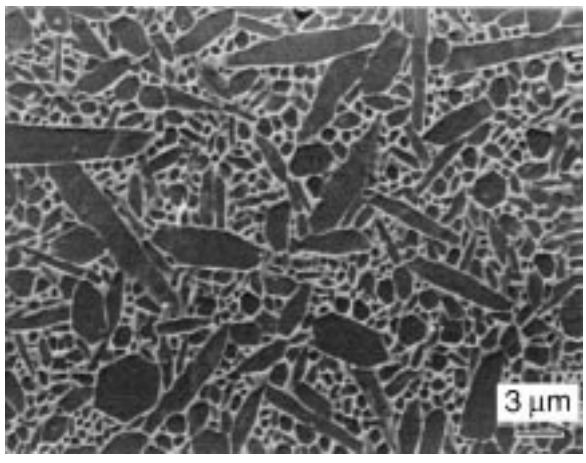

Fig. 1. The general microstructure of a dilute β sialon ceramic. Prismatic β' grains are separated by an Y, Al and O rich intergranular microstructure that appears bright in this scanning electron microscopy (SEM) image of a plasma etched section. (Courtesy of H. Björklund.)

2.2 Sialon ceramics

The intergranular volume fraction can be minimized through incorporation of liquid phase constituents into the solid phase during densification. α and β sialons are solid solutions based on the hexagonal α- and β-Si_3N_4 structures.[4,34–36] α sialon (α'-Si_3N_4) is isostructural with α-Si_3N_4 and has a composition given by $R_xSi_{12-(m+n)}Al_{m+n}O_nN_{16-n}$, where m(Si–N) are substituted by m(Al–N) and n(Si–N) by n(Al–O). The valency discrepancy introduced by this substitution is compensated for by the interstitial cation R^{p+}, and $x = m/p$. Cations such as Y^{3+}, Yb^{3+}, Dy^{3+}, Sm^{3+} and Nd^{3+} are well known to stabilize the α' structure.[4,36–41] β sialon (β'-Si_3N_4) forms when Si in the β-Si_3N_4 structure is substituted by Al, and some N at the same time is replaced by O for the retention of charge neutrality. The general formula of β sialon is $Si_{6-z}Al_zO_zN_{8-z}$, where $z \leq 4{\cdot}2$.[4,35,36] The Al and O and the α' stabilizing cation originate from metal oxide and nitride sintering additives.

Sialon systems are described by the Jänecke prism.[42,43] There is a a two-phase ($\alpha' + \beta'$) area on the α sialon plane between the α' solid solution and the linearly extended β sialon phase (Fig. 2). The sialon systems allow, hence, the fabrication of duplex α/β sialon ceramics with engineered *in-situ* reinforced microstructures containing prismatic β' grains dispersed in an α' matrix of higher hardness.[44–46] The duplex α/β sialons thus have a high potential as engineering ceramics.

3 High Resolution Imaging

The bonding between grains, and the grain boundary structure and chemistry, is of particular importance for mechanical, chemical and thermal behaviour.[3–6,15,16,47] A continuous intergranular glassy phase, present as thin grain boundary films, determines grain boundary strength, provides a rapid diffusion path, and may also promote grain re-arrangement and cavity formation under load at high temperatures.

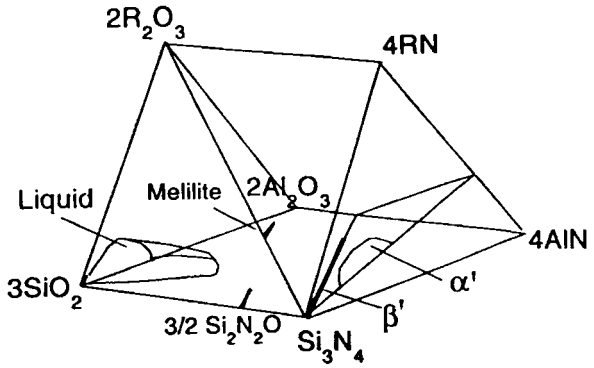

Fig. 2. Schematic illustration of the Jänecke prism of an R–Si–Al–O–N system.

There are a number of techniques for direct, and indirect, identification and imaging of grain boundary structures and intergranular films in the transmission electron microscope.[48–52] Larger volumes of residual glass, such as pockets at multi grain junctions, are easily identified in the TEM because of their lack of diffraction contrast when the thin foil is tilted under the electron beam. This technique is, however, not applicable when the glass is present as thin intergranular films.

3.1 Diffuse dark field imaging

The residual intergranular glassy phase may be directly imaged in dark field using the diffuse scattered electrons.[48,49] The electron beam is deflected off the optical axis and a portion of the halo formed by the diffuse scattered electrons is centered and selected by the objective aperture. In order to obtain good image contrast it is essential to eliminate any contribution from Bragg diffracted electrons from the surrounding grains. The glassy phase appears with bright contrast in this type of images (Fig. 3).

It has been shown that thickness measurement of edge-on grain boundary films imaged by this technique generally gives an overestimate of film thickness.[52] This could possibly be due to artefacts introduced during specimen preparation, like grain boundary grooving and re-deposition of sputtered matter during ion beam milling, as well as the presence of an evaporated C film on non-conducting Si_3N_4 and sialon foils. Specimen drift may be one other experimental error because of the need for long exposure times at high magnifications.

3.2 High resolution lattice imaging

High resolution lattice imaging is the only technique that resolves grain boundary detail with the resolution of an interplanar spacing in the crystal structures of the neighbouring grains.[48,49,52] The grain boundary must be in an edge-on orientation, and the adjacent grains must be in good diffracting conditions so that interference fringes are produced on either side of the film. The area of discontinuity in these fringes at the interface corresponds to the thickness of the intergranular film. Also, only the thinnest areas of the specimen can be used for imaging.

The lattice fringes are not localised. A change in defocus may cause the two sets of fringes to extend into the gap and obscure the grain boundary film.[48] This fringe shift with defocus is an electron optical effect that is microscope dependent. Images should, therefore, be recorded at different defoci close to

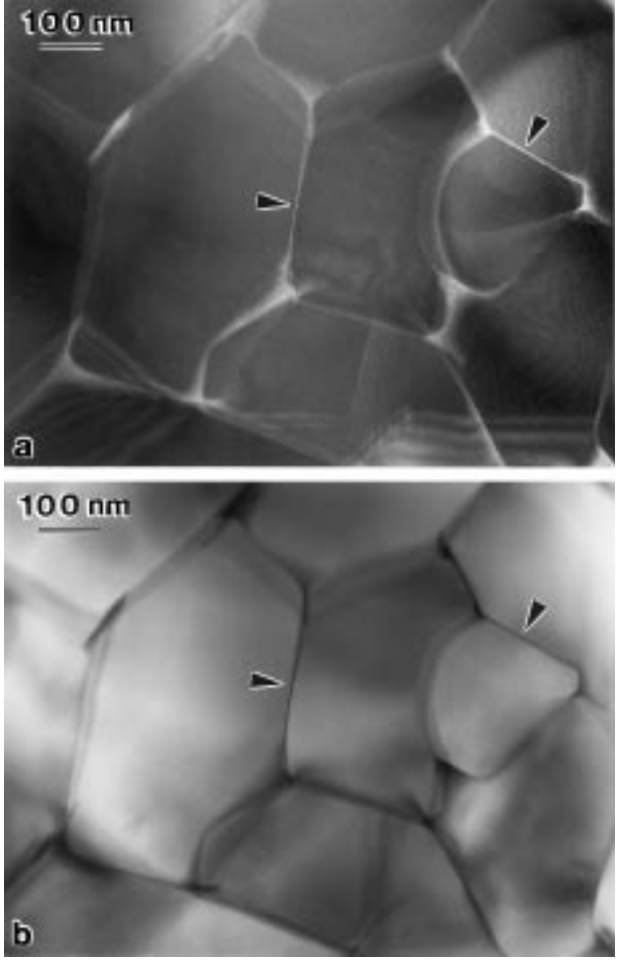

Fig. 3. (a) Centered dark field image formed from diffuse scattered electrons, and (b) the corresponding bright field TEM image. Thin films of residual glass (arrowed) separate the sialon grains in the microstructure of the Sm^{3+} stabilized duplex α/β sialon.

Scherzer and zero defocus. The grain boundary film thickness may then be determined from the spacing of the lattice fringes (Fig. 4).

3.3 Defocus Fresnel imaging

Defocus Fresnel imaging is an indirect technique for grain boundary film determination.[49–52] Fig. 5 shows Fresnel fringe contrast in images from a through focus series of a sialon grain boundary containing a thin amorphous film merging into a glassy pocket. The underfocus images contain a pair of dark lines delineating the boundary, and this contrast is reversed when going through Gaussian focus so that the overfocus images contain a pair of bright lines (arrowed in Fig. 5). There is reflection symmetry in the image intensity distribution if the grain boundary is oriented edge-on (Fig. 5). This may be used as an aid in grain boundary orientation which is very important in all microanalytical work.

The Fresnel fringes form because the grain boundary film introduces a phase shift that is proportional to the difference in mean inner

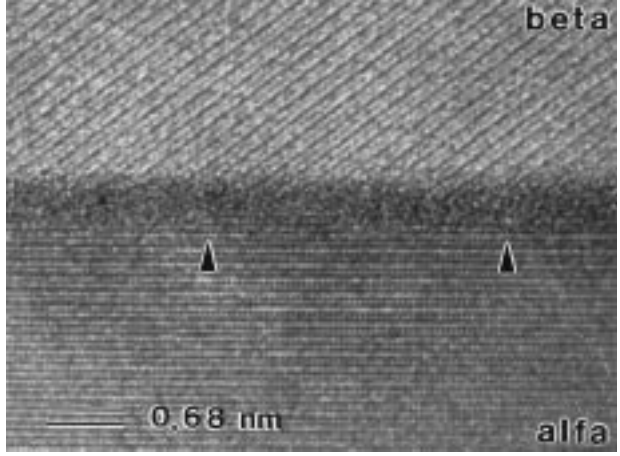

Fig. 4. High resolution lattice fringe image of an α'/β' grain boundary in the duplex sialon stabilized by Dy^{3+}. The transitions between the sialon grains and the glassy grain boundary film are not well defined, see arrows. The average film thickness was estimated to 2·3 nm from the spacing of the $\{10\bar{1}0\}$ fringes (interplanar spacing 0·676 > nm[45]) in the α' grain.

potential.[51] The first maximum or minimum fringe separation (W) depends on film thickness (t) and defocus (Δf) according to the relationship

$$W = t - (3\,\lambda\Delta f)^{1/2} \qquad (2)$$

where λ is the electron wavelength.[52] The grain boundary film thickness may be estimated from plots of fringe spacing as function of defocus. The intersection of plots of overfocus and underfocus series extrapolated to zero defocus represents the grain boundary film thickness (Fig. 6). There are, however, different experimental uncertainties with this technique. The Fresnel fringe visibility is strongly affected by the diffraction conditions in the grains on either side of the grain boundary film, and focus and image drift during recording of through-focus series will strongly affect the estimated film thickness.

4 Experimental Materials

4.1 Sialon ceramics

The α and duplex α/β sialon ceramics in the presented work were fabricated from balanced starting powder mixtures corresponding to the α-sialon composition $R_{0.4}Si_{10.2}Al_{1.8}O_{0.6}N_{15.4}$ (R = Sm, Dy or Yb) and the β-sialon composition $Si_{5.4}Al_{0.6}O_{0.6}N_{7.4}$. The duplex sialons had a starting powder composition corresponding to an α'/β' weight ratio of 1:1. The materials were hot-pressed in BN-coated graphite dies at 1800°C. The fabrication process of these sialon ceramics and their general microstructures and high temperature stability are discussed in Refs 44–46.

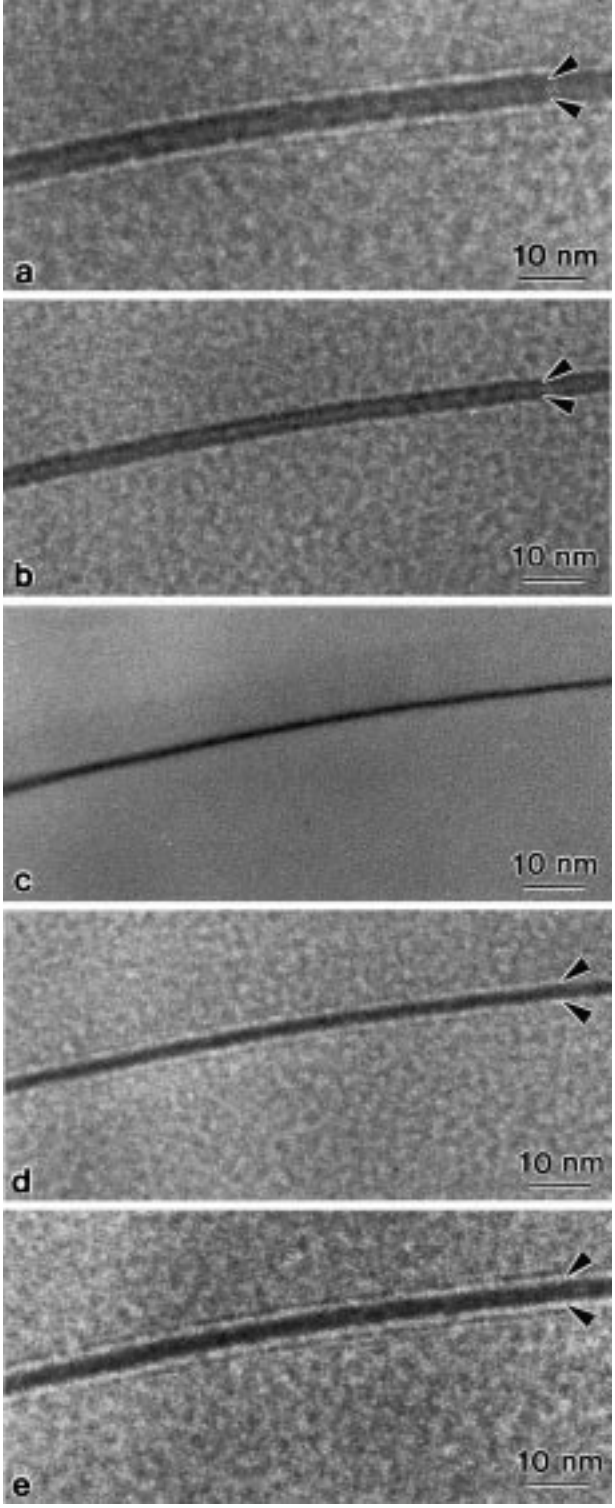

Fig. 5. Defocus Fresnel images of a grain boundary in the Dy^{3+} stabilized α sialon ceramic. Dy segregation to the glassy grain boundary film results in the absorption contrast in the image taken close to Gaussian focus (c). The underfocus images, (a) and (b), and the overfocus images, (d) and (e), are taken at approximate defoci of $-2{\cdot}6$ and $-1{\cdot}5\,\mu$m, and $+0{\cdot}8$ and $+1{\cdot}8\,\mu$m, respectively. First order minima (underfocus) and maxima (overfocus) are arrowed. Higher order Fresnel fringes are visible at large defoci, (a) and (e), because of the high coherency of the electron beam produced by the FEG.

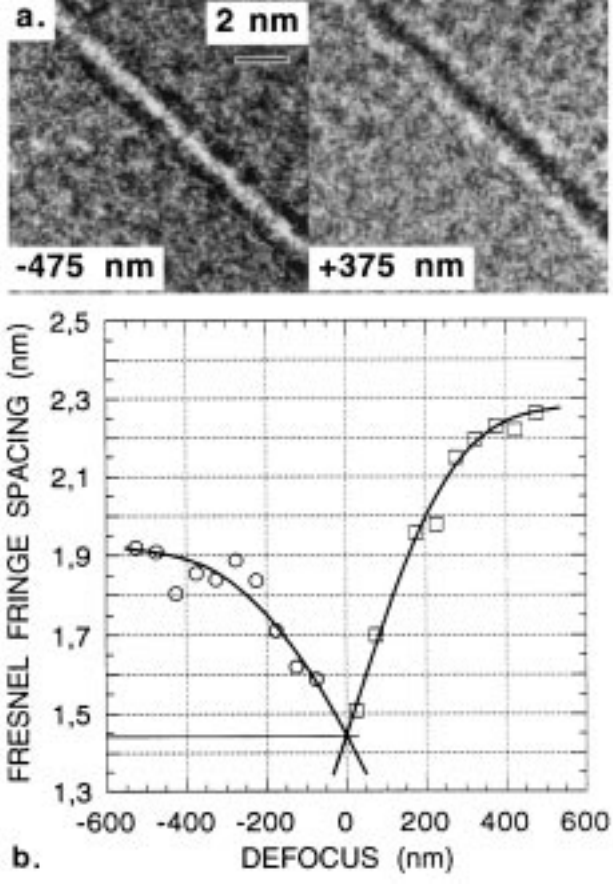

Fig. 6. Over- and underfocussed images of a SiC/SiC grain boundary showing (a) Fresnel fringe contrast, and (b) Fresnel fringe spacing as function of defocus. The film thickness was estimated to 1·4–1·5 nm.

4.2 SiC ceramics

The analysed α-SiC ceramics were fabricated with 3 wt% Al_2O_3 and Y_2O_3 with an Y_2O_3/Al_2O_3 molar ratio of 0·6. This ratio corresponds to that of the Y,Al-garnet, $5Al_2O_3{\cdot}3Y_2O_3$. The oxygen content of the SiC starting powder was equivalent to 2·1 wt% SiO_2. Green bodies were pressureless sintered or glass encapsulated and hot isostatically pressed (HIP). Pressureless sintering was carried out in a SiC/Al_2O_3 powder bed in an Ar atmosphere at 1880°C for 4 h, and HIP at 1800°C for 2 h under a pressure of 160 MPa. Detailed descriptions of the processing and densification procedures are given elsewhere.[25,53]

4.3 Specimen preparation for TEM

Thin foils for TEM were prepared from thin slices cut by a low speed diamond saw. The slices were ground and polished to a thickness of 100 to 120 μm, and 3 mm discs were cut by an ultrasonic drill. The discs were subsequently dimpled to a thickness of around 30 to 40 μm followed by ion beam thinning. Sputtering was carried out by 4 kV Ar ions at an incidence angle of 20°. A thin C film was evaporated onto the sialon foils, while the SiC foils were sufficiently conducting under the electron beam in the TEM and did not require any coating for imaging and analysis.

5 Microanalytical Techniques

5.1 Instrumentation

The work presented in this paper has been carried out on a Philips CM200 Super Twin TEM equipped with a Schottky field emitter. The microscope is also equipped with surrounding interactive instrumentation: the Gatan imaging filter (GIF) and the Link Isis EDX system with a super-ATW window in front of the detector allowing light element analysis.

The local chemistry was determined by EDX point analysis using a probe with a nominal FWHM of 0·7 nm, and grain boundary elemental profiles were established by point analysis in steps of 5 nm. Quantitative EDX analysis was carried out using the Link ISIS TEMQuant software. Elemental profiles for evaluation of peak area were acquired in the analytical configuration used for analysis, while the K_{XSi} values supplied by Link were used in quantification. Combined high resolution analytical and spatial information was obtained from electron energy filtered images, see Section 5.2.3 below.

5.2 Electron energy filtering

5.2.1 The electron energy loss spectrum

The electrons undergo both elastic and inelastic scattering processes on their way through the thin foil.[54] The inelastic scattering results in a certain loss in electron energy. The zero loss peak, which mainly contains the unscattered and the elastically scattered electrons with energy E_0, is the most intense feature in the energy spectrum of the transmitted electrons (Fig. 7). This peak is followed by the plasmon peak which contains electrons that have suffered energy losses arising from interactions with weakly bond electrons. The remaining part of the EEL spectrum consists of element characteristic edges superimposed on a background that is rapidly decreasing towards higher energy losses. The ionization edges are caused by excitation of inner shell electrons, and the exact position of the edge and the edge structure provides information on the elemental environment and the valence state.

5.2.2 Instrumentation

When an energy selecting slit is placed in a plane containing a focussed EEL spectrum, it is possible to select certain electron energy losses for imaging. Such electron spectroscopic images combine spatial and elemental information.[19–21,55]

The Gatan imaging filter (GIF) is a post-column energy filter that is attached to the bottom flenge of the TEM column.[19,20] The filter consists basically

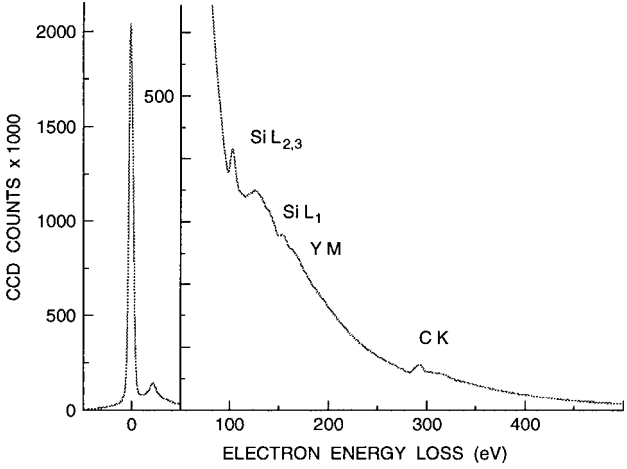

Fig. 7. EEL spectrum from the HIP:ed SiC ceramic.

of two stages (Fig. 8). The first stage focusses on the final crossover after the last projector lens in the TEM column. This stage contains a magnetic prism that produces an EEL spectrum that is focussed onto a plane containing a retractable energy selecting slit. The second stage of the filter contains quadrupole and sextupole lenses that either transform the EEL spectrum back into an electron image, or produce an image of the spectrum with an energy dispersion that can be varied.

The filter can thus be used for qualitative and quantitative electron energy loss spectroscopy (EELS) and production of electron energy filtered diffraction patterns and images. In zero loss imaging, the unscattered and elastically scattered electrons with energy E_0 are selected by the slit.[20,55] This improves image contrast because the inelastically scattered electrons that are defocused due to the chromatic aberration of the objective lens are filtered away.[55] When imaging with electrons that have suffered a certain energy loss ΔE, the high tension in the TEM is increased from E_0 to $E_0 + \Delta E$ by the image filter control software.[19,20] In this way, focus is maintained and the energy

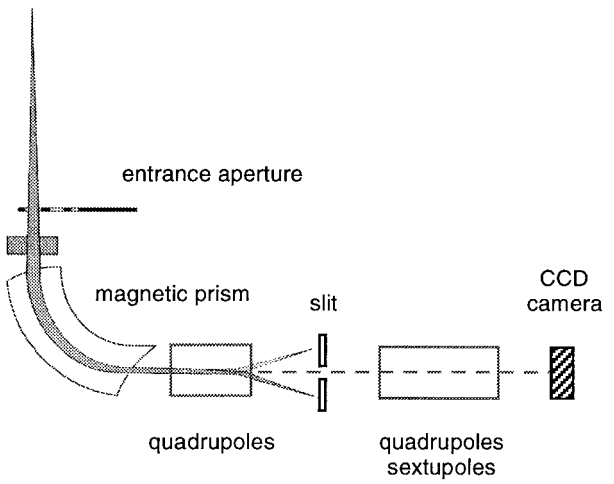

Fig. 8. Schematic showing the main components of the GIF.

selecting slit is still centered around the electron energy E_0.

A slow scan CCD camera for parallel recording of spectra and digital images is integrated in the GIF. Also unfiltered images and diffraction patters may be recorded since the energy selecting slit is retractable.

The digital images presented in this paper were acquired with a binning factor of 2, resulting in 512×512 pixels, and processed with the Gatan software DigitalMicrograph. The acquired images were corrected for dark current and gain variations.

5.2.3 Elemental distribution images

Two types of elemental distribution images may be obtained from electron energy filtered images, elemental maps and jump ratio maps. Elemental maps are computed by subtracting a background image, calculated from two pre-edge images, from a post-edge image containing the element specific signal.[21–23,55] Different mathematical models are supplied with the Gatan software Digital Micrograph in order to extrapolate the EEL spectral background under element specific edges. The power-law model was applied in the present work. The background intensity in the post-edge image was calculated according to

$$I = AE^{-r} \quad (3)$$

where E is the energy loss and the A and r parameters are calculated pixel by pixel from the two pre-edge images.[55]

Elemental maps of C and N were calculated from electron energy filtered images recorded around the K edges using an energy selecting slit width of 30 eV for C and 20 eV for N. The distribution of O in the SiC ceramics was also displayed as elemental maps, and appropriate energy losses around the O K edge were selected for imaging by a 40 eV slit. The computation of an oxygen elemental map from the electron energy filtered images is shown in Figs 9 and 10. The three electron spectroscopic images, acquired with the slit centered around energy losses of 472, 512 and 552 eV, are shown in Fig. 10 together with the computed O elemental map.

Jump ratio maps are computed by dividing a post-edge image by a pre-edge image.[23] Artefacts that may be introduced by background modeling and subtraction are avoided by this method, and diffraction contrast cancells out. Also, jump ratios result in elemental distribution images with a better signal to noise ratio.[23]

Because of the presence of N, the O distribution in the sialon materials was displayed as the ratio

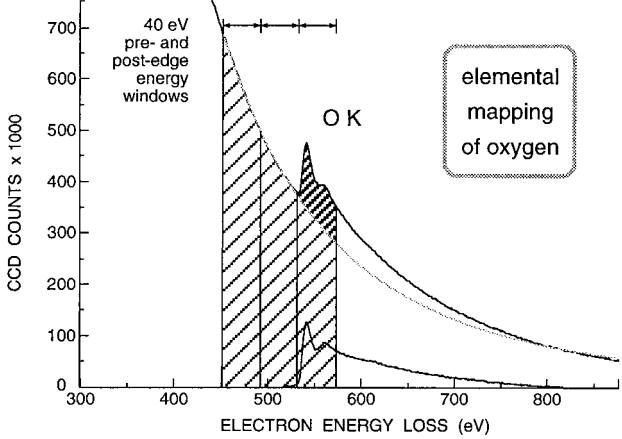

Fig. 9. Selection of electron energy losses for image acquisition around the O K edge.

between the post-edge and the pre-edge 2 images (Fig. 9). The Al and rare earth element distributions were also displayed as jump ratio maps. The deleyed Al $L_{2,3}$ edge has a low signal to background ratio, and the rare earth element $N_{4,5}$ edges are situated just above the Si L edges in the EEL spectrum. Electron spectroscopic images acquired for computing of an Al jump ratio map is shown in Fig. 11. The images were recorded around the Al $L_{2,3}$ edge using a slit width of 20 eV centered around energy losses of 63 and 83 eV. A slit width of 20 eV was used also for energy filtered imaging around the rare earth element $N_{4,5}$ edge.

Any drift between successive energy filtered images recorded for computation of the elemental distribution images was corrected for by the software.

6 α-SiC Microstructures

The variation in SiC grain morphology within the two microstructures imply that a solution/reprecipitation process occurred in certain volumes of the compacts during densification. Larger intergranular pockets contained grains with small and rounded sections while the surrounding, larger, SiC grains had a faceted shape (Fig. 12). The major part of the α-SiC grains, including the faceted grains, had the 6H polytype; there was only a limited transformation to 2H and 15R during densification.[25] Elemental concentration profiles across edge-on grain boundary films and SiC/glass interfaces did not reveal any incorporation of Y, Al or O into the α-SiC grains from the liquid phase sintering medium. This is in contrast to work on SiC ceramics sintered at the slightly higher temperature 1950°C; these α-SiC 6H grains had a core/rim structure where the rim contained smaller amounts of dissolved Y, Al and O.[56]

Intergranular Y,Al-garnet did not form in the HIP:ed SiC ceramic, despite the balanced metal

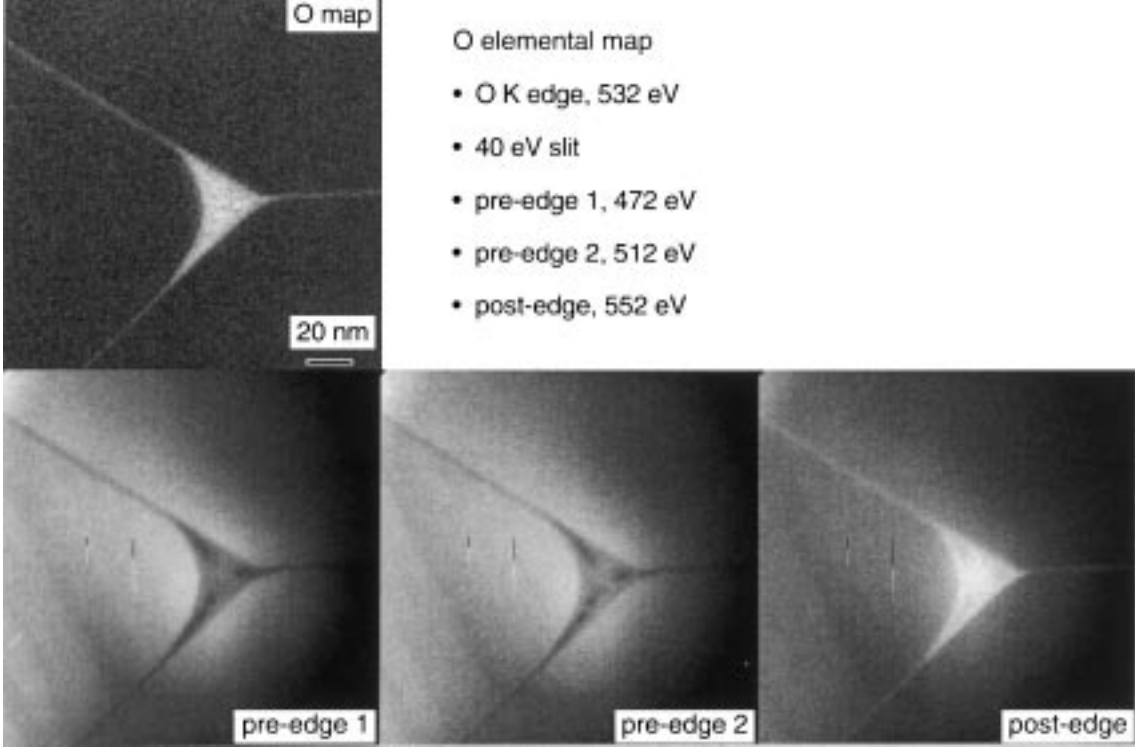

Fig. 10. The computation of an O elemental map from electron energy filtered images. This is a triple grain junction in the HIP:ed SiC ceramic.

oxide addition to the starting powder mixture, [Fig. 12(b)]. A continuous Y, Al, Si and O rich glassy phase, with significant variations in its cation content, was present as thin intergranular films merging into pockets at multi grain junctions (Fig. 13). The elemental distribution images of the triple grain junction in Fig. 13 show the segregation of Al and O to the intergranular glass and also that the glass was lean in C. It proved difficult to map the Y distribution in these microstructures; the Y M edge is too close to the Si L_1 edge in the

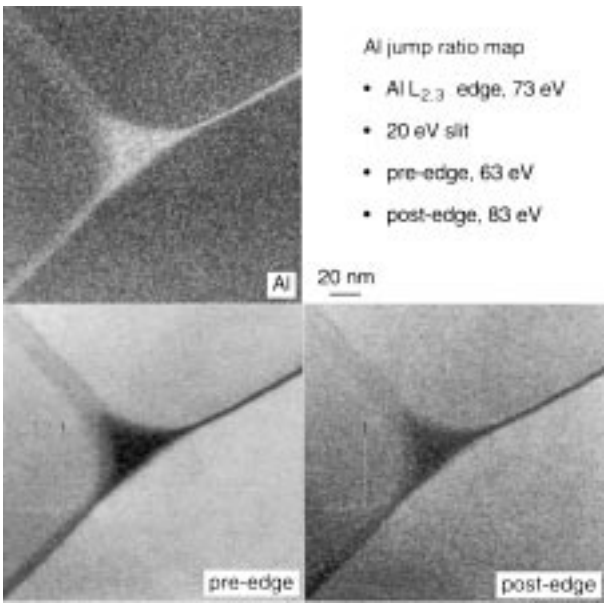

Fig. 11. The computation of an Al jump ratio map from electron energy filtered images. This is a triple grain junction in the α sialon ceramic stabilized by Sm^{3+}.

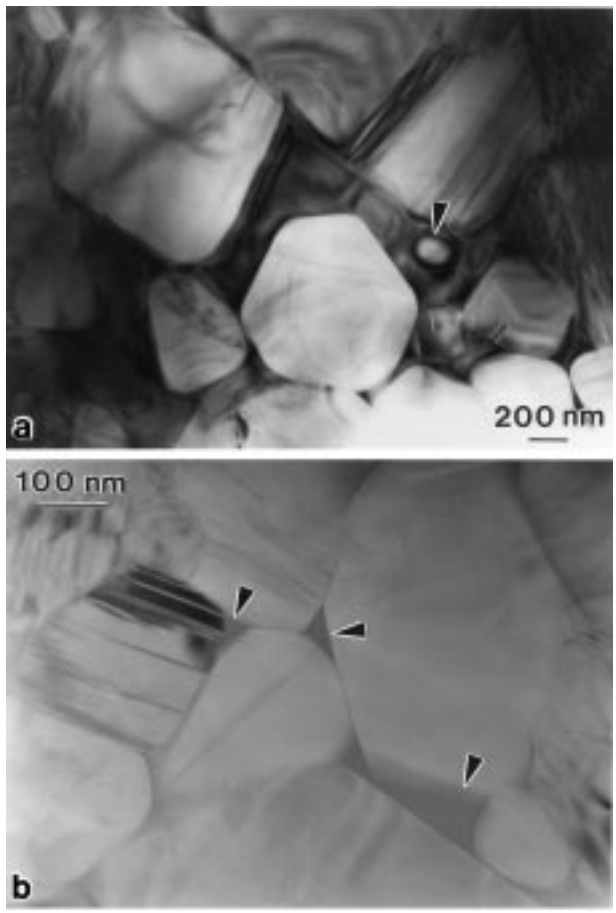

Fig. 12. General microstructures of the liquid phase sintered α-SiC ceramic after (a) pressureless sintering and (b) HIP. A smaller SiC grain section with rounded shape (arrowed) is present in the Y,Al-garnet in (a). A continuous intergranular glassy phase (arrowed) showing absorption contrast due to its Y content is present in (b).

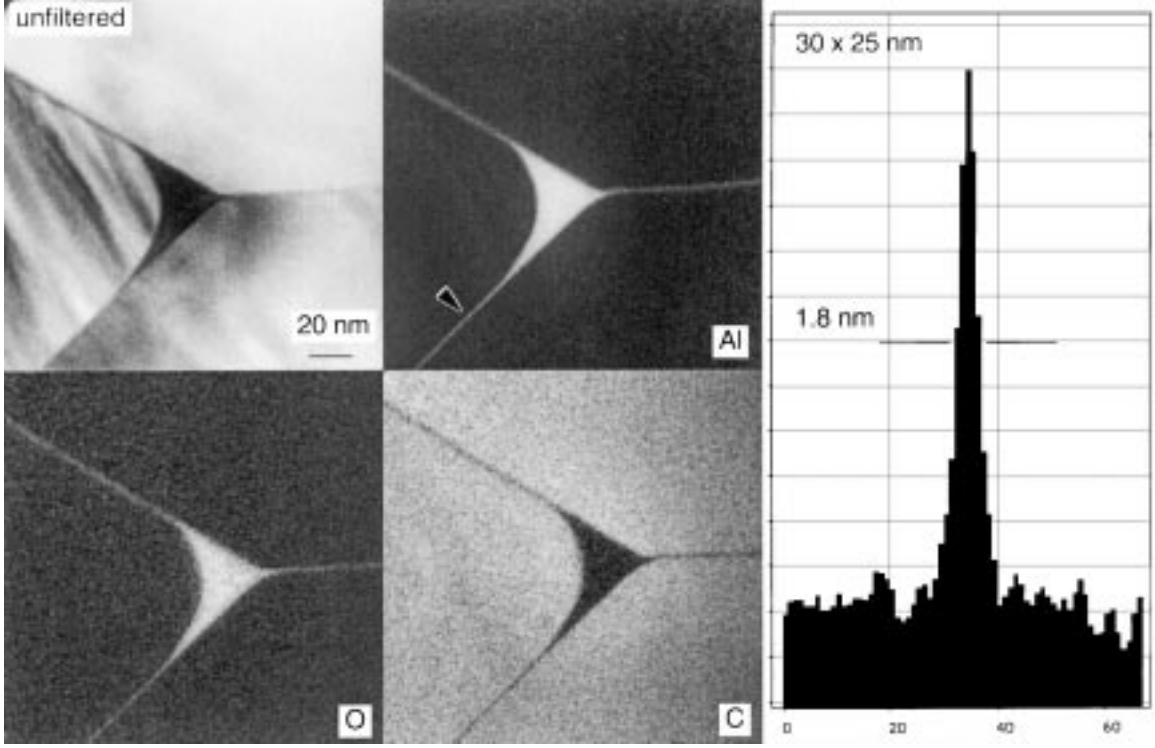

Fig. 13. Elemental distribution images of the HIP:ed SiC ceramic. The computation of the O elemental map is shown in Figs 9 and 10. The intensity distribution in the Al image across the edge-on grain boundary (arrowed) was integrated over 30 nm of the boundary. (The numbers on the x-axis are channel numbers. The total number of channels corresponds to a length of 25 nm at right angle across the grain boundary.)

EEL spectrum. The intensity profile integrated along 30 nm of the edge-on grain boundary in the Al image (arrowed in Fig. 13) had a FWHM of 1·8 nm. EDX point analysis showed that this grain boundary film had a Y/Al atomic ratio of 0·59, which is very close to that of the Y,Al-garnet (Y/Al = 0·60).

Densification by HIP proceeds in a closed system which means that the overall composition of the starting powder mixture is retained in the sintered material. A number of the analysed glass pockets also had Y/Al atomic ratios around 0·60 which indicates that the retention of the liquid phase sintering medium as a residual intergranular glassy phase was determined by other factors than composition.[31,57,58] The stress/strain state in the body due to the applied high pressure during densification as well as the cooling rate from the densification temperature will affect the degree of equilibrium crystallisation.[57,58]

Two crystalline intergranular phases formed in the pressureless sintered SiC ceramic, α-Al_2O_3 and Y,Al-garnet ($5Al_2O_3{\cdot}3Y_2O_3$). The formation of α-Al_2O_3 was promoted by the transport of Al_2O_3, associated with vapor phase reactions, from the surrounding Al_2O_3/SiC powder bed.[25,26] Partitioning of the Y,Al-garnet from the liquid phase sintering medium resulted in intergranular pockets with the same crystallographic orientation over larger areas in the microstructure. This morphology implies that the crystallisation involved comparatively few nucleation sites, and that the garnet grew in a three-dimensional intergranular network. The pockets were, however, not fully crystallised; thin amorphous films were separating the garnet from the surrounding SiC grains.[25,26]

Thin amorphous films were always present at SiC/SiC grain boundaries also in the pressureless sintered material. Fine probe EDX analysis showed that these films were rich in Al and O, but Y could not be detected in glassy grain boundary films merging into pockets containing the Y,Al-garnet. This implies that the crystallisation of the garnet depleted the remaining liquid of Y, and thereby caused a shift towards a SiO_2–Al_2O_3 composition of the residual liquid/glass.

The thickness of an Al and O rich glassy grain boundary film was estimated to 1·4 to 1·5 nm from defocus Fresnel imaging (Fig. 6). The Fresnel fringe spacing at different defoci was determined from unfiltered digital images of the grain boundary acquired with the CCD camera integrated in the GIF. Intensity profiles were integrated over a grain boundary length of around 30 nm. The separation between fringe first maxima or minima in these integrated profiles was determined form the magnification of the imaging system, and the change in defocus between acquired images was read from the microscope.

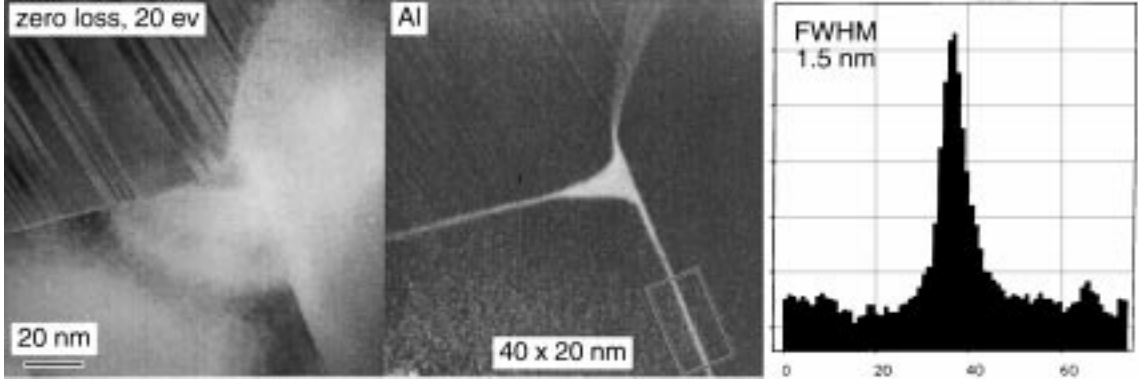

Fig. 14. A zero loss image and an Al jump ratio map of intergranular glass films merging into a small glass pocket at a triple grain junction in the pressureless sintered SiC ceramic. The intensity profile was integrated along 40 nm of the edge-on grain boundary in the Al map. (The numbers on the x-axis are channel numbers. The total number of channels corresponds to a length of 20 nm at right angle across the grain boundary; see box area in the Al map.)

A limited number of smaller pockets of residual glass was also present in the intergranular microstructure of the pressureless sintered material (Fig. 14). These pockets were rich in Si, Al and O, and contained smaller amounts of Y (< 1 cation%) and generally also Ca impurity cations. The Y contents of these glassy pockets was thus far too low for crystallisation of the Y,Al-garnet. Glassy grain boundary films merging into these pockets also contained very low amounts of Y and the impurity cation, in addition to the Al and O. A 20 nm wide intensity profile integrated along 40 nm of the Al image of the edge on grain boundary in Fig. 14 (arrowed) had a FWHM of 1·5 nm.

7 Sialon Microstructures

The crystallisation of secondary phases in sialon ceramics is controlled by the overall composition, the α' stabilizing cation and the temperature/time programme during densification.[4,32,40,41,44,46] The formation of duplex α/β sialon microstructures makes it possible to reduce the intergranular volume fraction, but fully crystalline microstructures have not been obtained despite the extensive solid solutions of the α' and β' structures and densification of compacts with chemically balanced starting powder compositions.[44–46] A certain volume fraction of the liquid phase sintering medium was always retained as a continuous residual intergranular glassy phase in the characterized α and duplex α/β sialon microstructures. The glass was in some cases, however, present only as very thin intergranular films.[46] This would, then, support theoretical models that predict an equilibrium thickness of the intergranular glassy films; attractive van der Waals forces are balanced by repulsive, film structure dependent, forces.[59,60]

Elemental distribution images clearly revealed the concentration of the α' stabilizing cation, Al and O to the intergranular glass and also that the glass had a reduced N content. This is illustrated in Fig. 15, which shows triple grain junctions between α' grains in an α sialon ceramic stabilized by Sm^{3+} and a duplex α/β sialon stabilized by Dy^{3+}. The residual glass is present as thin grain boundary films merging into smaller pockets at multi grain junctions. The displayed segregation of cations to the glassy grain boundary films in the microstructures of these sialon ceramics was confirmed by EDX point analysis. Atomic ratio profiles across a grain boundary in the Sm^{3+} stabilized α sialon and across an α'/β' boundary in the duplex α/β sialon stabilized by Dy^{3+} are shown in Fig. 16.

The intergranular microstructure of the Sm^{3+} stabilized α sialon also contained a significant volume fraction of Al substituted Sm melilite, $Sm_2Si_{3-x}Al_xO_{3+x}N_{4-x}$.[45] This phase did not form in the duplex α/β sialon stabilized by Sm^{3+} which may be explained by the presence of two sialon phases with extensive solid solutions which would enable local accommodation of chemical variations.

A zero loss image of a boundary between an α' and a β' grain in the duplex sialon stabilized by Yb^{3+} is shown in Fig. 17. The film thickness was constant along the grain boundary, and determined to 1·6 nm from the $\{10\bar{1}0\}$ fringes (interplanar spacing of 0·66 nm[46]) in the β' grain. Elemental concentration profiles across this grain boundary showed an increased concentration of Al and Yb in the glassy grain boundary film [Fig. 18 (a)]. The α and β sialon substitution levels given in Fig. 17 were calculated from the average cation compositions of the sialon grains according to the general formulae given in Section 2·2 above. The local cation content of the α' and β' grains varied however significantly, but there were no obvious concentration gradients within the grains up to the grain boundary film [Fig. 18(a)]. Analysed α'/α' and β'/β' boundaries in this duplex sialon ceramic

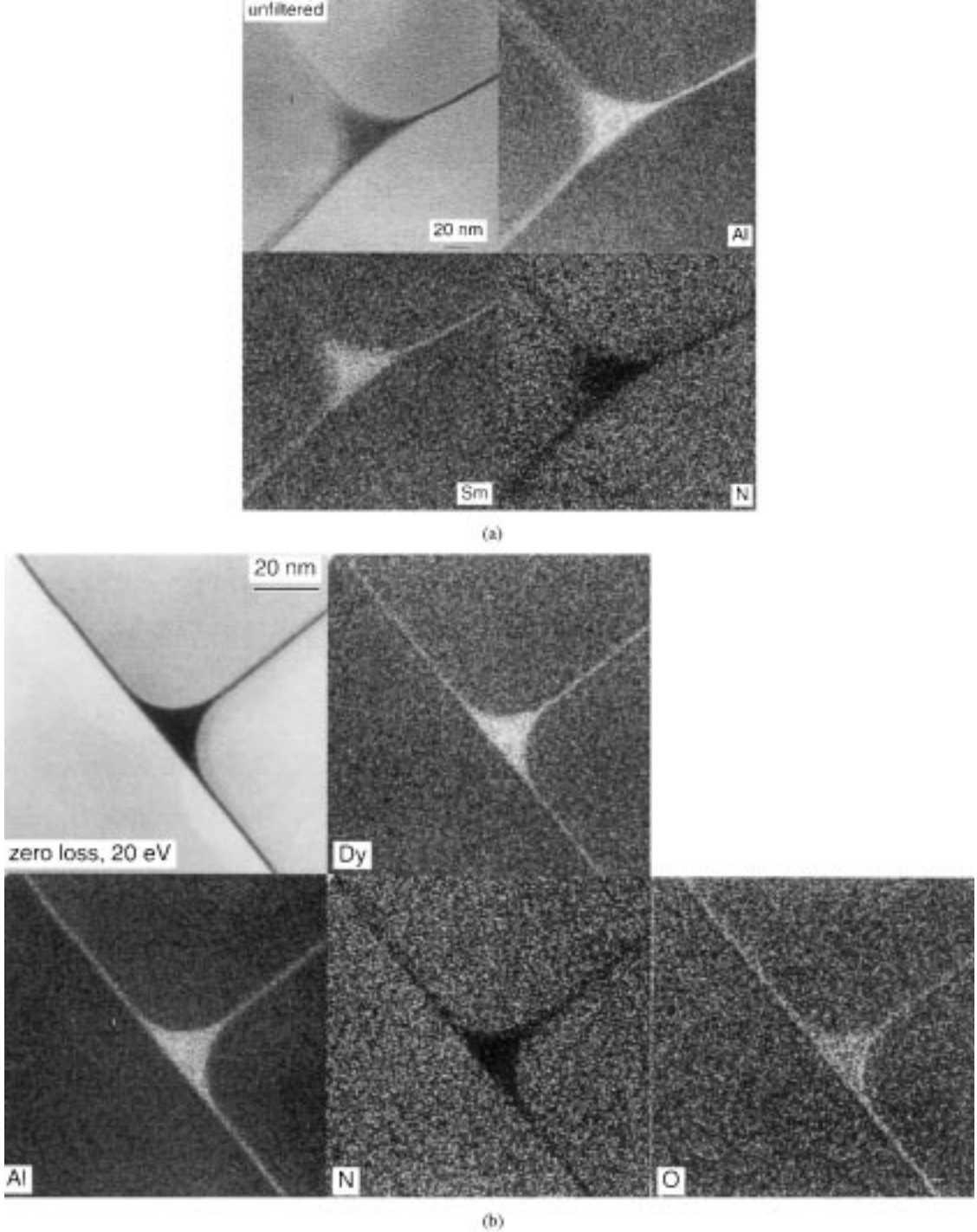

Fig. 15. Elemental distribution images of triple grain junctions between α' grains in the α sialon ceramic stabilized by (a) Sm^{3+} and (b) the duplex α/β sialon stabilized by Dy^{3+}. The computation of the Al jump ratio image in (a) is shown in Fig. 11.

showed that there was always an enrichment of the additive cations to the glassy grain boundary film, and that there was a significant variation in the local sialon substitution level, both within and between grains of the same structure [Fig. 18(b) and (c)]. This behaviour is also shown by the EDX results presented in Fig. 16. The variations in the local α and β sialon cation contents reflect the extensive solid solution ranges of the α and β sialon structures.

The cation ratios displayed at the grain boundary films in Figs 16 and 18 should, however, not be taken as absolute figures. Beam spreading in the thin foils will inevitably result in a limited contribution from the adjacent sialon grains to the grain boundary analyses, i.e. the true cation ratios of the grain boundary glass should be slightly higher. The beam spreading in an individual point analysis acquired for construction of the grain boundary profiles was typically in the range 1·5 to 2·5 nm as calculated by the Link ISIS TEMQuant software.

α' substitution levels calculated from the EDX results using the general formula $R_xSi_{12-(m+n)}$

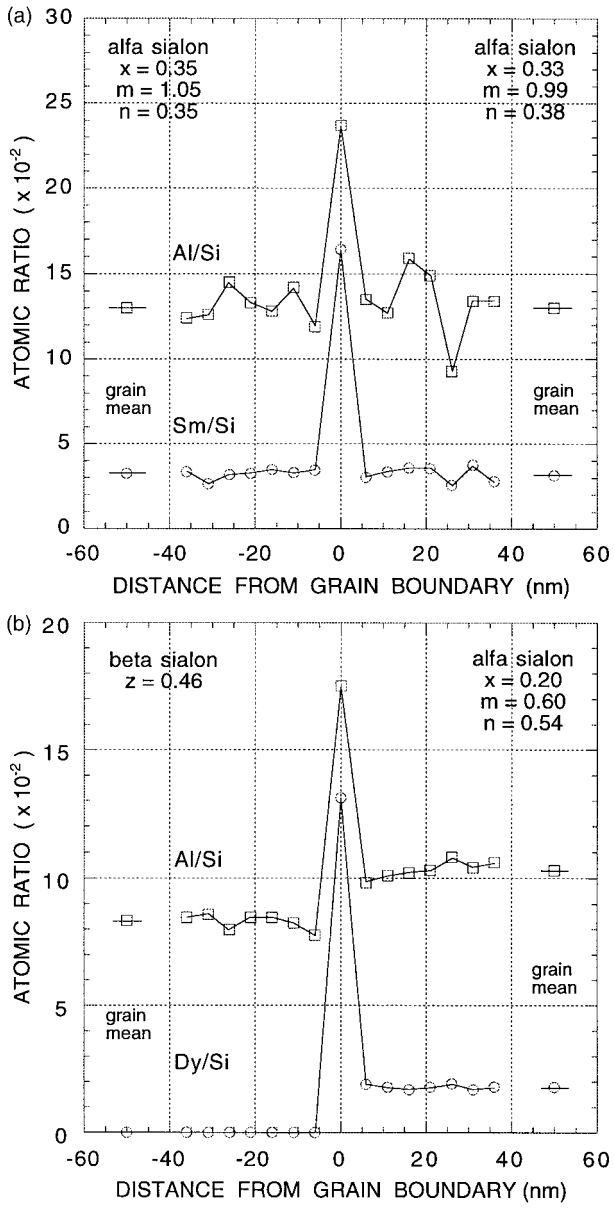

Fig. 16. Atomic ratio profiles obtained from step by step EDX point analysis across (a) a grain boundary in the Sm^{3+} stabilized α sialon and (b) an α'/β' boundary in the duplex α/β sialon stabilized by Dy^{3+}. The indicated sialon substitution levels were determined from grain mean cation compositions.

$Al_{m+n}O_nN_{16-n}$, thus assuming a constant valence state of the rare earth cations, indicated that a smaller cation radius will extend the range of substitution levels to smaller x-values, i.e. towards the β-sialon solid solution. The smaller radius of Yb^{3+} (0·858 Å) gave x-values as low as 0·13, while the lowest x-values in analysed α' grains stabilized by Dy^{3+} (0·908 Å) or Sm^{3+} (0·964 Å) were 0·17 and 0·26, respectively. Local x-values lower than that aimed at by the starting powder composition ($x = 0{\cdot}40$) is consistent with the presence of a cation rich intergranular volume.

The composition of the glass pockets in these sialon microstructures varied significantly between different areas. The glass composition was, however, always more cation rich than the surrounding sialon grains. It has been shown previously that the intergranular chemistry in a particular part of the microstructure is related to the local α' and β' phase assemblage and substitution levels.[46]

There was also a significant variation in cation content within a glassy pocket (Fig. 19). The α sialon grain did not reveal any variation in cation composition associated with the growth front on the $\{10\bar{1}0\}$ prism plane, but there were clear diffusion profiles away from the interface into the residual glass. A comparatively low additive cation content, particularly the Sm concentration, close to the interface was followed by a significant increase in the Al and Sm concentrations before the glass composition levelled out. A continued sialon grain growth requires the presence of adequate amounts of Si and N and the incorporation of Al, O and the α' rare earth stabilizing cation would be determined by the local overall chemistry. Excess cation species that are not incorporated into the sialon structure have to diffuse away from the moving interface into the remaining liquid volume. This would result in the observed higher rare earth and Al concentrations of the glass outside the α' grain. The grain growth rate would, hence, be influenced by the self diffusivity of the oxynitride liquid phase constituents at the densification temperature.

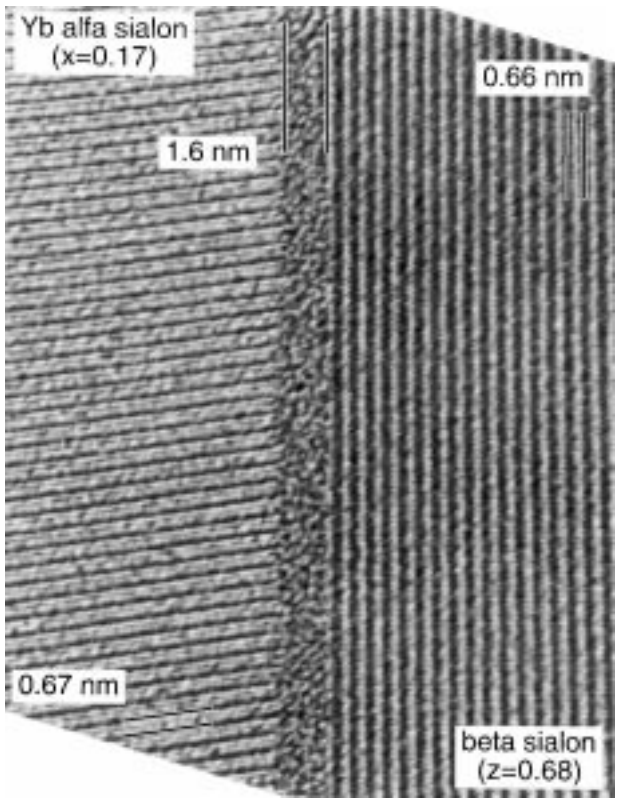

Fig. 17. Zero loss image of a boundary between an α' and a β' grain in the duplex sialon stabilized by Yb^{3+}. The indicated sialon substitution levels were determined from grain mean cation compositions.

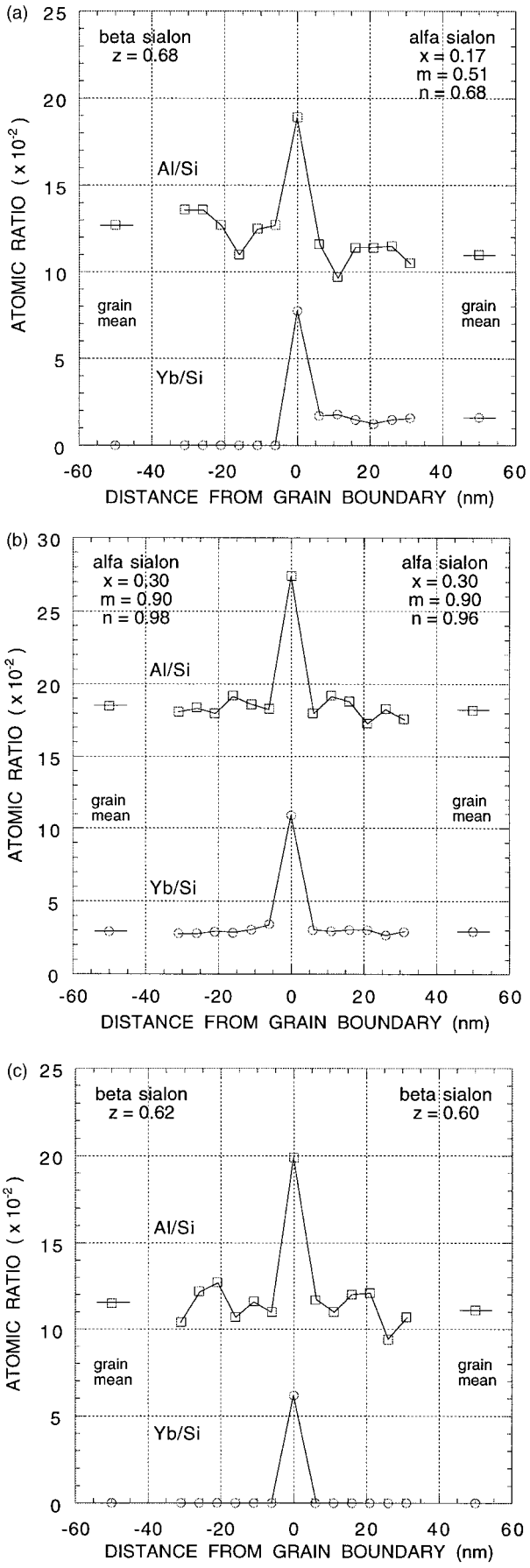

Fig. 18. Atomic ratio profiles obtained from step by step EDX point analysis across three different types of grain boundaries in the duplex sialon stabilized by Yb^{3+}. (a) The α'/β' grain boundary imaged in Fig. 17, (b) an α'/α' and (c) a β'/β' grain boundary.

Similar diffusion profiles in pockets of residual glass have been observed in a dilute β sialon ceramic densified with the addition of Y_2O_3.[61]

Zero loss imaging enhances image contrast as shown by the images of an edge-on α'/β' grain boundary in the duplex sialon stabilized by Yb^{3+} (Fig. 20). The zero loss image was acquired with an energy selecting slit of 20 eV. The absorption contrast due to the segregation of Yb to the glassy grain boundary film makes it possible to estimate film thickness from the unfiltered and zero loss images although only the α' grain was in a strongly diffracting orientation. The α'/glass interface was not abrupt, but the average film thickness was estimated to 1·9 nm from intensity profiles across the grain boundary in these images. The jump ratio map across the Yb N edge shows the concentration of Yb to the glassy grain boundary film, and also that phase contrast may be preserved in electron

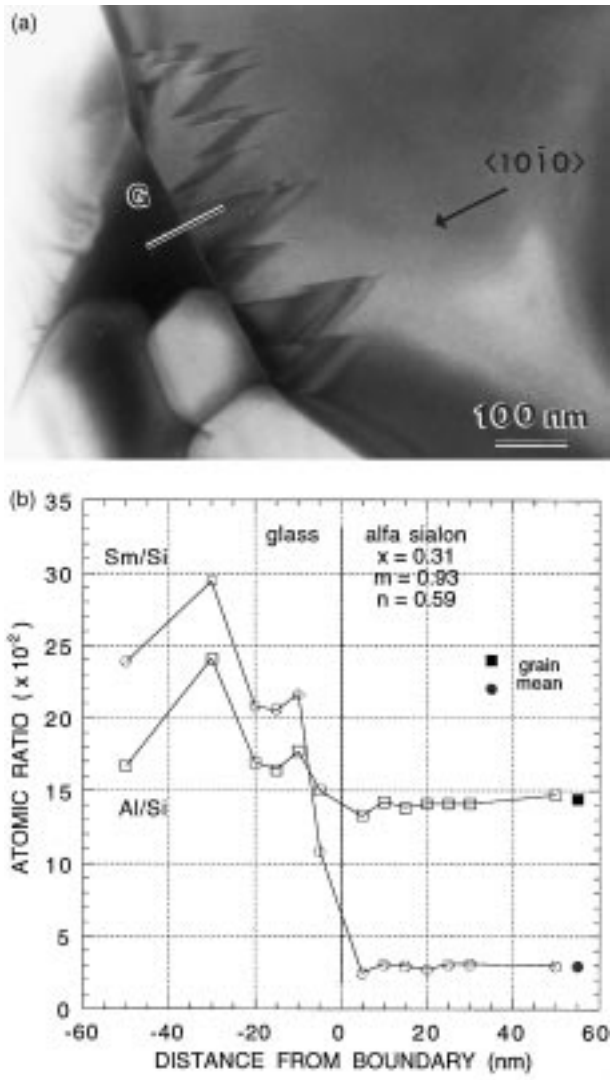

Fig. 19. α' grain growth into surrounding liquid at high temperature. Atomic ratio profiles obtained from step by step EDX point analysis across the prism plane/glass (G) interface as indicated in (a) are shown in (b). This is the α sialon material stabilized by Sm^{3+}.

energy filtered images and computed elemental distribution images. The preservation of phase

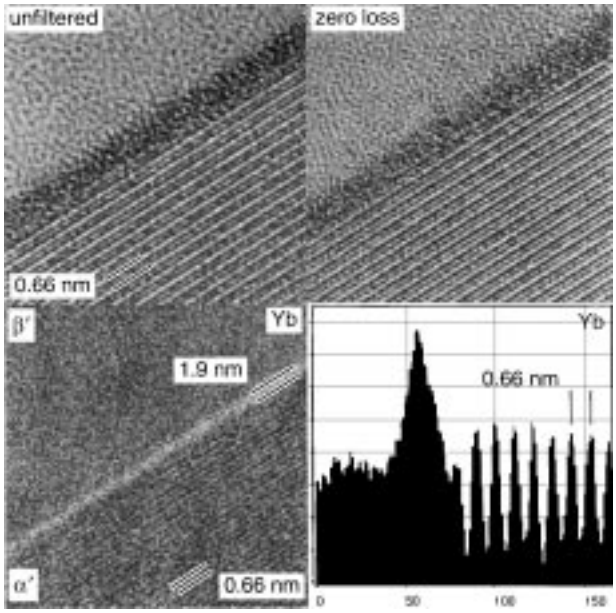

Fig. 20. Unfiltered and zero loss images of an edge-on α'/β' grain boundary in the duplex sialon stabilized by Yb^{3+}. The zero loss image was acquired with an energy selecting slit of 20 eV. The jump ratio map across the Yb N edge (lower magnification) shows the concentration of Yb to the glassy grain boundary film and the preservation of phase contrast in the α' grain. The grain boundary film thickness was estimated to 1·9 nm from a 10 nm intensity profile integrated along 30 nm of the grain boundary in the Yb jump ratio map. (The numbers on the x-axis are channel numbers.)

contrast in low electron energy loss images, which is due to Bragg scattering of inelastically scattered electrons, has been described previously.[55,62] The grain boundary film thickness was estimated to 1·9 nm from a 10 nm intensity profile integrated along 30 nm of the grain boundary in the Yb jump ratio map using the α' $\{10\bar{1}0\}$ lattice fringes (interplanar spacing of 0·66 nm[46]) for internal calibration. This value of the film thickness is, hence, consistent with the measurements on the unfiltered and zero loss images.

The average substitution levels of the sialon grains in Fig. 20 were significantly different from those in Fig. 17. The α sialon x-value was higher, 0·25 instead of 0·17, while the β sialon z-value was as low as 0·35. Also, the estimated grain boundary film thickness was slightly increased in the more rare earth rich area (Fig. 20). Further work is required in order to establish whether the indicated difference in α'/β' grain boundary film thickness is inherent to measurement on different types of images or to a different local chemistry. A change in sialon substitution levels, as well as variations in local film composition, would affect the force balance across the grain boundary and thereby the equilibrium film thickness.[63]

Grain boundary film thickness determination from lattice fringes in a zero loss and the corresponding Al jump ratio map, where both grains are in strongly diffracting condition, is shown in Fig. 21.

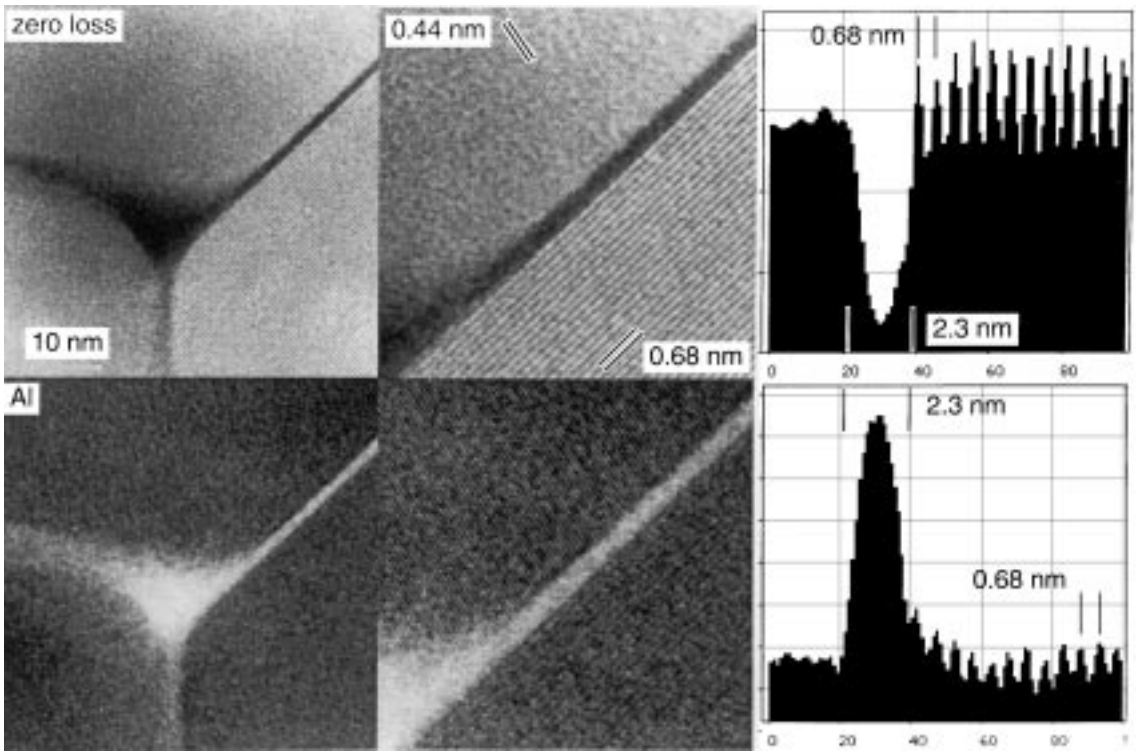

Fig. 21. Zero loss images and Al jump ratio maps of an edge on grain boundary merging into a glassy pocket at a triple grain junction in the α sialon ceramic stabilized by Sm^{3+}. The intensity profiles across the edge-on grain boundary film in the zero loss (top) and Al jump ratio (bottom) images were integrated along 15 nm of the boundary. (The numbers on the x-axes are channel numbers.)

This is a triple grain junction in the α sialon ceramic stabilized by Sm^{3+}, and the segregation of Sm to the intergranular glass results in strong absorption contrast in the zero loss image. The local chemistry was not determined in this particular area, but the Al content of analysed α' grains in this sialon ceramic was in the range 8·2 to 13·2 cation% while the average compositions of the glass pockets were around 16 cation% Al. Intensity profiles were integrated along 15 nm of the edge-on grain boundary film in the zero loss image and the Al jump ratio map see Fig. 21. The same number of channels in these profiles were attributed to the film, and the film thickness was determined to 2·3 nm using the $\{10\bar{1}0\}$ lattice fringes for internal calibration. The average $\{10\bar{1}0\}$ interplanar spacing in this α sialon ceramic was determined to 0·68 nm from X-ray diffraction data.[45] This, and the previous, example shows that phase contrast preserved during electron spectroscopic imaging and subsequent computation of elemental distribution images allows an accurate size determination of chemically distinct fine scale features such as the thickness of grain boundary films with increased cation contents.

8 Concluding Remarks

The combined information from different imaging, diffraction and spectroscopic methods in the TEM is required for qualitative and quantitative chemical and structural characterization of small volumes in liquid phase sintered ceramic microstructures. Electron spectroscopic imaging and subsequent computation of elemental distribution images makes it possible to obtain analytical and spatial information from regions of the size 1 to 2 nm. Phase contrast may be preserved in electron energy filtered images and computed elemental maps which allows an accurate size determination of chemically distinct fine scale features. The characterization of grain boundaries in α and duplex α/β sialon microstructures imply that not only the α' stabilizing cation radius but also the local chemistry and the type of grain boundary will determine the equilibrium film thickness.

Acknowledgements

The experimental materials were supplied by the Swedish Ceramic Institute and the Department of Inorganic Chemistry, University of Stockholm. Financial support was received from the Swedish Research Counsil for Engineering Sciences.

References

1. Lange, F. F., Silicon nitride polyphase systems: fabrication, microstructure and properties. *Int. Met. Rev.*, 1980, **1**, 1–20.
2. Lange, F. F., Fabrication and properties of dense polyphase silicon nitride. *J. Am. Ceram. Soc. Bull.*, 1983, **62**, 1369–1374.
3. Ziegler, G., Heinrich, J. and Wötting, G., Review: relationships between processing, microstructure and properties of dense and reaction-bonded silicon nitride. *J. Mater. Sci.*, 1987, **22**, 3041–3086.
4. Jack, K. H., Silicon nitride, sialons, and related ceramics. In *Ceramics and Civilization, Vol. III, High-Technology Ceramics*, ed. W. D. Kingery. American Ceramic Society, Columbus, OH, 1986, pp. 259–288.
5. Jou, Z. C., Virkar, V. and Cutler, R. A., High temperature creep of SiC densified using transient liquid phase. *J. Mater. Res.*, 1991, **6**, 1945–1949.
6. Raj, R., Fundamental research in structural ceramics for service near 2000°C. *J. Am. Ceram. Soc.*, 1993, **76**, 2147–2174.
7. Cutler, R. A. and Jackson, T. B., Liquid phase sintered silicon carbide. In *Proceedings of the 3rd International Symposium on Ceramic Materials and Components for Engines*, ed. V. J. Tennery. American Ceramic Society, Westerville, OH, 1989, pp. 309–318.
8. Alliegro, R. A., Coffin, L. B. and Tinklepaugh, J. R., Pressure-sintered silicon carbide. *J. Am. Ceram. Soc.*, 1956, **39**, 386.
9. Tanaka, H., Sintering of silicon carbide. In *Silicon Carbide Ceramics*, ed. S. Somiya and Y. Inomata. Elsevier Applied Science, London, 1991, pp. 213–238
10. Lewis, M. H. and Lumby, R. J., Nitrogen ceramics: liquid phase sintering. *Powder Metallurgy*, 1983, **26**, 73–81.
11. Cordrey, L., Niesz, D. E. and Shanefield, J., Sintering of silicon carbide with rare-earth oxide additions. In *Sintering of Advanced Ceramics*, ed. C. A. Handwerker, J. E. Blendell and W. Kaysser. The American Ceramic Society, Westerville, Ohio, 1990, pp. 618–636.
12. Lewis, M. H., Leng-Ward, G. and Jasper, C., Sintering additive chemistry in controlling microstructure and properties of nitrogen ceramics. *Ceram. Powder Sci.*, 1988, **2**, 1019–1033.
13. Falk, L. K. L. and Rundgren, K., Microstructure and short term oxidation of hot-pressed Si_3N_4/ZrO_2 ($+Y_2O_3$) ceramics. *J. Am. Ceram. Soc.*, 1992, **75**(1), 28–35.
14. Knutson-Wedel, M., Falk, L. K. L. and Ekström, T., Characterization of Si_3N_4 ceramics formed with different oxide additives. *J. Hard Materials*, 1992, **3**(3–4), 435–445.
15. Becher, P. F., Microstructural design of toughened ceramics. *J. Am. Ceram. Soc.*, 1991, **74**, 255–269.
16. Karunaratne, B. S. B. and Lewis, M. H., High-temperature fracture and diffusional deformation mechanisms in Si–Al–O–N ceramics. *J. Mater. Sci.*, 1980, **15**, 449–462.
17. Knutson-Wedel, E. M., Falk, L. K. L., Björklund, H. and Ekström, T., Si_3N_4 ceramics formed by HIP using different oxide additions–relations between microstructure and properties. *J. Mater. Sci.*, 1991, **26**, 5575–5584.
18. Tuersley, I. P., Leng-Ward, G. and Lewis, M. H., High-temperature Si_3N_4 ceramics. In *Engineering with Ceramics*, ed. R. Morrell. British Ceramic Society, 1990, pp. 231–246.
19. Krivanek, O. L., Gubbens, A. J., Dellby, N. and Meyer, C. E., Design and first applications of a post-column imaging filter. *Microsc. Microanal. Microstruct.*, 1992, **3**, 187–199.
20. Gubbens, A. J. and Krivanek, O. L., Applications of a post-column imaging filter in biology and materials science. *Ultramicroscopy*, 1993, **51**, 146–159.
21. Mayer, J., Berger, A. and Kohl, H., Electron spectroscopic imaging and its applications to thin film analysis. In *Electron Microscopy 1994, Volume 1: Interdisciplinary*

Developments and Tools, ed. B. Jouffrey and C. Colliex. Les Éditions de Physique Les Ulis, Les Ulis Cedex A, France, 1994, pp. 615–620.
22. Berger, A., Mayer, J. and Kohl, H., Detection limits in elemental distribution images produced by energy filtering TEM: case study of grain boundaries in Si_3N_4. *Ultramicroscopy*, 1994, **55**, 101–112.
23. Hofer, F., Grogger, W., Kothleitner, G. and Warbichler, P., Quantitative analysis of EFTEM elemental distribution images. *Ultramicroscopy*, 1997, **67**, 83–103.
24. Hampshire, S. and Jack, K. H., The kinetics of densification and phase transformation of nitrogen ceramics. In *Special Ceramics* 7, ed. D. Taylor and P. Popper. British Ceramic Research Association, Stoke-on-Trent, UK, 1981, pp. 37–49.
25. Falk, L. K. L., Microstructural development during liquid phase sintering of silicon carbide ceramics. *J. Eur. Ceram. Soc.*, 1997, **17**, 983–994.
26. Falk, L. K. L., Intergranular microstructure of liquid phase sintered SiC ceramics. In *Ceramics: Charting the Future*, ed. P. Vincenzini. Techna Srl, 1995, pp. 1925–1932.
27. Björklund, H., Falk, L. K. L., Rundgren, K. and Wasén, J., β–Si_3N_4 grain growth, Part I: effect of metal oxide additives. *J. Eur. Ceram. Soc*, 1997, **17**, 1285–1299
28. Björklund, H. and Falk, L. K. L., Grain morphology and intergranular microstructure of whisker reinforced Si_3N_4 ceramics. *J. Eur. Ceram. Soc.*, 1997, **17**, 13–24.
29. Pyzik, A. J. and Beaman, D. R., Microstructure and properties of self-reinforced silicon nitride. *J. Am. Ceram. Soc.*, 1992, **75**, 259–276.
30. Wötting, G., Feuer, H. and Gugel, E., The influence of powders and processing methods on microstructure and properties of dense silicon nitride. In *Silicon Nitride Ceramics: Scientific and Technological Advances*, ed. I.-W. Chen, P. F. Becher, M. Mitomo, G. Petzow and T.-S. Yen. Materials Research Society, Pittsburgh, PA, 1993, pp. 133–146.
31. Falk, L. K. L. and Dunlop, G. L., Crystallisation of the glassy phase in a Si_3N_4 material by post-sintering heat treatments. *J. Mater. Sci.*, 1987, **22**, 4369–4376.
32. Thompson, D. P., New grain-boundary phases for nitrogen ceramics. In *Silicon Nitride Ceramics: Scientific and Technological Advances*, ed. I.-W. Chen, P. F. Becher, M. Mitomo, G. Petzow and T.-S. Yen. Materials Research Society, Pittsburgh, PA, 1993, pp. 79–92.
33. Clarke, D. R. and Lange, F. F., Oxidation of Si_3N_4 alloys: relation to phase equilibria in the system Si_3N_4–SiO_2–MgO. *J. Am. Ceram. Soc.*, 1980, **63**, 586–593.
34. Hampshire, S., Park, H. K., Thompson, D. P. and Jack, K. H., α-sialon ceramics. *Nature (London)*, 1978, **274**, 880–882.
35. Jack, K. H., The characterization of α-sialons and the α–β relationships in sialons and silicon nitrides. In *Progress in Nitrogen Ceramics*, ed. F. L. Riley. Martinus Nijhoff, The Hague, 1983, pp. 45–60.
36. Ekström, T. and Nygren, M., Sialon ceramics. *J. Am. Ceram. Soc.*, 1992, **75**, 259–276.
37. Sun, W. Y., Tien, T. Y. and Yen, T.-S., Solubility limits of α-sialon solid solutions in the system Si, Al, Y/N, O. *J. Am. Ceram. Soc.*, 1991, **74**, 2547–2550.
38. Cheng, Y. B. and Thompson, D. P., Preparation and grain boundary devitrification of samarium α-sialon ceramics. *Journal of the European Ceramic Society*, 1994, **14**, 13–21.
39. Shen, Z.-J., Ekström, T. and Nygren, M., Homogeneity region and thermal stability of neodymium doped α-sialon ceramics. *J. Am. Ceram. Soc.*, 1996, **79**, 721–732.
40. Mandal, H. and Thompson, D. P., Reversible $\alpha \leftrightarrow \beta$ sialon transformation in heat-treated sialon ceramics. *J. Eur. Ceram. Soc.*, 1993, **12**, 421.
41. Camuscu, N., Thompson, D. P. and Mandal, H., Effect of starting composition, type of rare earth sintering additive and amount of liquid phase on $\alpha \leftrightarrow \beta$ sialon transformation. *J. Eur. Ceram. Soc.*, 1997, **17**, 599–613.
42. Jack, K. H., The relationship of phase diagrams to research and development of sialons. In *Phase Diagrams: Materials Science and Technology*, Vol. V, ed. A. M. Alper. Academic Press, New York, 1978, pp. 242–285.
43. Gaukler, L. J. and Petzow, G. P., Representation of multicomponenet silicon nitride based systems. In *Nitrogen Ceramics*, ed. F. L. Riley. Noordhoff, Leyden, 1977, pp. 41–60.
44. Falk, L. K. L., Shen, Z.-J. and Ekström, T., α–β sialon ceramics in the Dy–Si–Al–O–N and Sm–Si–Al–O–N systems. In *Fourth Euro Ceramics*, Vol. 2, ed. C. Galassi. Gruppo Editoriale Faenza Editrice S.p.A., Faenza, Italy, 1995, pp. 163–168.
45. Ekström, T., Falk, L. K. L. and Shen, Z.-J, Duplex α–β sialon ceramics stabilized by dysprosium and samarium. *J. Am. Ceram. Soc.*, 1997, **80**, 301.
46. Falk, L. K. L., Shen, Z.-J. and Ekström, T., Microstructural stability of duplex α–β sialon ceramics. *J. Eur. Ceram. Soc.*, 1997, **17**, 1099–1112.
47. Pezzotti, G., Ota, K. and Kleebe, H.-J., Grain-boundary relaxation in high-purity silicon nitride. *J. Am. Ceram. Soc.*, 1996, **79**, 2237–2246.
48. Krivanek, O. L., Shaw, T. M. and Thomas, G., Imaging of thin intergranular phases by high-resolution electron microscopy. *J. Appl. Phys.*, 1979, **50**, 4223–4227.
49. Clarke, D. R., On the detection of thin intergranular films by electron microscopy. *Ultramicroscopy*, 1997, **4**, 33–44.
50. Clarke, D. R., Observation of microcracks and thin intergranular films in ceramics by transmission electron microscopy. *J. Am. Ceram. Soc.*, 1980, **63**, 100–106.
51. Ness, J. N., Stobbs, W. M. and Page, T. F., A TEM Fresnel diffraction-based method for characterizing thin grain-boundary and interfacial films. *Phil. Mag. A*, 1986, **54**, 679–702.
52. Cinibulk, M. K., Kleebe, H.-J. and Rühle, M., Quantitative comparison of TEM techniques for determining amorphous intergranular film thickness. *J. Am. Ceram. Soc.*, 1993, **76**, 426–432.
53. Kahlman, L., Rundgren, K., Lidén, E., Nyberg, B. and Carlström, E., Processing of liquid phase sintered SiC–mechanical and wear properties. In *Third Euro-Ceramics V.3*, ed. P. Duran and J. F. Fernandez. Faenza Editrice Ibérica S. L., Castellon de la Plana, 1993, pp. 477–482.
54. Egerton, R. F., *Electron Energy Loss Spectroscopy in the Electron Microscope*, 2nd edn. Plenum Press, New York, 1996.
55. Reimer, L., Electron spectroscopic imaging. In *Energy-Filtering Transmission Electron Microscopy*, ed. L. Reimer. Springer–Verlag, Berlin, Heidelberg, 1995, pp. 347–400.
56. Sigl, L. S. and Kleebe, H.-J., Core/rim structures of liquid-phase-sintered silicon carbide. *J. Am. Ceram. Soc.*, 1993, **76**, 773–776.
57. Raj, R. and Lange, F. F., Crystallisation of small quantities of glass (or liquid) segregated in grain boundaries. *Acta Metallurgica*, 1981, **29**, 1993–2000.
58. Kessler, H., Kleebe, H.-J., Cannon, R. W. and Pompe, W., Influence of internal stresses on crystallization of intergranular phases in ceramics. *Acta Metall. Mater.*, 1992, **40**, 2233–2245.
59. Clarke, D. R., On the equilibrium thickness of intergranular glass phases in ceramic materials. *J. Am. Ceram. Soc.*, 1987, **70**, 15–22.
60. Clarke, D. R., Shaw, T. M., Philipse, A. P. and Horn, R. G., Possible electrical double-layer contribution to the equilibrium thickness of intergranular glass films in

polycrystalline ceramics. *J. Am. Ceram. Soc.*, 1993, **76**, 1201–1204.
61. Björklund, H. and Falk, L. K. L., β-Si_3N_4 grain growth, Part II: Intergranular glass chemistry. *J. Eur. Ceram. Soc.*, 1997, **17**, 1301–1308.
62. Wang, Z. L., Lattice imaging using plasmon energy-loss electrons in an energy-filtered transmission electron microscope. *Ultramicroscopy*, 1997, **67**, 105–111.
63. Bergström, L., Meurk, A., Arwin, H. and Rowcliffe, D. J., Estimation of Hamaker constants of ceramic materials from optical data using lifshitz theory. *J. Am. Ceram. Soc.*, 1996, **79**, 339–348.